

Ross Sea Ice Motion, Area Flux, and Deformation

R. Kwok

Jet Propulsion Laboratory, California Institute of Technology, Pasadena, California

(Manuscript received 8 November 2004, in final form 31 March 2005)

ABSTRACT

The sea ice motion, area export, and deformation of the Ross Sea ice cover are examined with satellite passive microwave and RADARSAT observations. The record of high-resolution synthetic aperture radar (SAR) data, from 1998 and 2000, allows the estimation of the variability of ice deformation at the small scale (~ 10 km) and to assess the quality of the longer record of passive microwave ice motion. Daily and subdaily deformation fields and RADARSAT imagery highlight the variability of motion and deformation in the Ross Sea. With the passive microwave ice motion, the area export at a flux gate positioned between Cape Adare and Land Bay is estimated. Between 1992 and 2003, a positive trend can be seen in the winter (March–November) ice area flux that has a mean of $990 \times 10^3 \text{ km}^2$ and ranges from a low of $600 \times 10^3 \text{ km}^2$ in 1992 to a peak of $1600 \times 10^3 \text{ km}^2$ in 2001. In the mean, the southern Ross Sea produces almost twice its own area of sea ice during the winter. Cross-gate sea level pressure (SLP) gradients explain $\sim 60\%$ of the variance in the ice area flux. A positive trend in this gradient, from reanalysis products, suggests a “spinup” of the Ross Sea Gyre over the past 12 yr. In both the NCEP–NCAR and ERA-40 surface pressure fields, longer-term trends in this gradient and mean SLP between 1979 and 2002 are explored along with positive anomalies in the monthly cross-gate SLP gradient associated with the positive phase of the Southern Hemisphere annular mode and the extrapolar Southern Oscillation.

1. Introduction

The present examination of sea ice motion, area flux, and deformation pertains to a much larger problem: the formation of dense water in the Ross Sea. Divergent motion in the Ross Sea produces areas of sea ice growth in leads and polynyas, which dominate the heat flux into the atmosphere and salt flux into the ocean. Along the continental margins, total brine flux and dense water production are related to this ice growth and export. Dense, high-salinity water produced here sinks along the continental slope after mixing with surrounding waters ([Foster and Carmack 1976](#); [Gordon 1991](#)) to form the Antarctic Bottom Water (AABW) of the deep ocean. Modeling studies ([Toggweiler and Samuels 1995](#); [Goosse and Fichefet 1999](#)) have highlighted the importance of brine rejection during the formation of sea ice on large-scale salinity and the role of the ice cover in the Southern Ocean circulation regime. At present, no consensus exists regarding the location and rates at which deep water is being produced in the Southern Ocean ([Broecker et al.](#)

[1998](#)). The best-documented sources lie along the margins of the Weddell Sea. Sources of dense bottom water have been identified at other locations around the perimeter of Antarctica, such as the Adelie Coast, and off Enderby Land. The Ross Sea, in the Pacific sector, is also thought to be a significant source of this cold high-salinity water.

While it is clear that the Ross Sea ice cover plays a key role in modifying the atmosphere–ocean interactions in exchanges of heat, mass, and momentum, present knowledge of this ice cover is rather limited and is well summarized by [Jeffries and Adolphs \(1997\)](#). The Ross Sea ice cover varies seasonally from a typical minimum of $0.8 \times 10^6 \text{ km}^2$ during the summer to a maximum of $3.8 \times 10^6 \text{ km}^2$ during the austral winter ([Gloersen et al. 1992](#)). The ice cover is primarily seasonal, forming in the southern zones as early as March and melting during mid-November–December. The Ross Sea and Terra Nova Bay polynyas ([Bromwich et al. 1998](#); [van Woert 1999](#)), and the Ross Sea Passage and Pennell Bank polynyas ([Jacobs and Comiso 1989](#)), where intense atmosphere–ocean interactions take place, have been identified as sites with significant heat and salt fluxes associated with new ice growth. In terms of systematic observations, for over two decades satellite passive microwave (PMW) retrievals have generally provided a large-scale view, albeit at low resolution, of the ice cover in terms of its extent and concentration. The great strengths of this PMW dataset are its spatial coverage and the length of the data record that is over 20 yr for the combination of the Scanning Multifrequency Microwave Radiometer (SMMR) and the Special Sensor Microwave Imager (SSM/I). Some of the inferences of the ice cover properties that have been drawn from this dataset can be found in [Jacobs and Comiso \(1989\)](#). In the winter, the uncertainties in the retrieval are fairly high and are reported to be $\sim 6\%$, with possible biases of similar magnitude. In the summer, snow wetness and surface melt introduce additional complications in the retrieval ([Cavalieri 1992](#)). Near the coast or ice front, because of the size of the footprint of these radiometers, the brightness temperature of the sea ice or open-ocean samples could be contaminated by the spillover from adjacent samples that have different signatures.

There is a paucity of ice motion observations for examining the large-scale, advective part of the circulation and the small-scale nonuniform motion responsible for the formation of leads and pressure ridges. Using buoy drift, some general characteristics of large-scale ice motion in the Ross Sea have been documented by [Moritz \(1988\)](#). In recent years, a number of investigators have developed procedures for extraction of ice motion from PMW observations ([Agnew et al. 1997](#); [Liu and Cavalieri 1998](#); [Kwok et al. 1998](#)). [Venegas et al. \(2001\)](#) used PMW ice drift to examine the coupled oscillations in sea ice and atmosphere in the Pacific sector, but summaries of the quality and utility of the derived ice motion for analysis of the Ross Sea ice cover have not been published. Measurements for understanding the small-scale spatial and temporal characteristics of motion and deformation are not generally available. Data on snow and ice thickness distributions and growth processes in the pack ice are limited to small areas and brief periods ([Jeffries and Weeks 1992](#); [Jeffries et al. 1994](#); [Jeffries and Adolphs 1997](#); [Tin and Jeffries 2001](#)). Except for ice extent and concentration, no dataset exists for development of detailed climatologies of the ice cover.

Recent changes in this Ross Sea region are compelling. Between 1982 and 1998, there is a negative trend in the ice edge in the Pacific sector north of the Ross Sea and a positive trend immediately west of this region ([Kwok and Comiso 2002](#)). Over the past four decades, [Jacobs et al. \(2002\)](#) report marked decreases in the High-salinity shelf water (HSSW)—the densest water mass in the Southern Ocean—and the surface salinity within the Ross Gyre. These hydrographic changes have been accompanied by atmospheric warming on Ross Island and ocean warming at depths of ~ 300 m north of the continental shelf. To understand the consequences of these changes, longer and coordinated records of hydrographic and sea ice measurements will be needed to assess the significance of apparent trends in the regional air temperature and HSSW over recent decades.

The behavior of sea ice is coupled to the large-scale climate. Coupled variability of recent Southern Ocean climate and sea ice behavior was summarized as a circumpolar wave pattern in [White and Peterson \(1996\)](#). Connections to extrapolar climate are reported by [Yuan and Martinson \(2000\)](#) and [Kwok and Comiso \(2002\)](#). In particular, [Kwok and Comiso \(2002\)](#) found the strongest correlation between the Southern Oscillation and the polar climate and sea ice anomalies in the Bellingshausen, Amundsen, and Ross Seas. The potential for melting sea ice and ice sheets in Antarctica associated with global warming could cause changes of these southern deep-water sources. The increased poleward moisture flux due to warming results in increased precipitation in the high latitudes, which in concert with ice melt, could enhance the meltwater impact on ocean circulation.

Our contribution to this topic is our present analysis of the motion, area flux, and deformation of the Ross Sea ice cover using ice motion derived from available PMW and RADARSAT imagery. The longer record of the PMW ice motion allows us to examine the variability of ice motion and area flux over a 12-yr period (1992–2003) and to explore their connections to larger-scale atmospheric circulation. The ice motion from high-resolution RADARSAT imagery, though a more limited dataset, provides a glimpse of the variability of motion and deformation at the 10-km scale and a means for assessing the quality of the longer record of PMW ice motion. [Section 2](#) describes the datasets and our assessment of the SSM/I ice motion by comparison with RADARSAT ice motion. [Section 3](#) summarizes the winter PMW and RADARSAT motion fields. [Section 4](#) discusses the variability in area flux, the velocity profiles at the flux gate, and the uncertainties of these estimates. Linkages of the Ross Sea surface pressure distribution and ice flux to the Southern Oscillation and the Southern Hemisphere annular mode are explored in [section 5](#). The kilometer-scale deformation of the Ross Sea ice cover is discussed in [section 6](#). Daily and a small subset of subdaily RADARSAT ice motion allow a glimpse at the spatial dependence and temporal variability of the motion and deformation of the ice cover. [Section 7](#) gives our conclusions.

2. Data description


a. Dataset: RADARSAT and PMW motion

Ice motion from satellite PMW observations is derived using the procedure described in ([Kwok et al. 1998](#)). Specifically, only the winter (March–November sea ice season) daily motion fields from the 85-GHz V-polarization channel (the resolution is ~ 12.5 km) are used in the analyses that follow as ice-tracking results are unreliable during the summer and transitional months: this is due to variability in the brightness temperature fields associated with water vapor, cloud liquid content, and surface wetness during the summer. This daily 85-GHz dataset spans a 12-yr period between 1992 and 2003. Even though data from this channel are available prior to 1992, they are not used because of the frequent coverage gaps.

Daily and a limited number of subdaily ice motion fields are derived using available RADARSAT synthetic aperture radar (SAR) imagery (the resolution is ~ 150 m) acquired during the austral winter of 1998 and 2000. Subdaily observations are possible at the latitude of the Ross Sea near the ice front; the convergence of the satellite ground tracks and the RADARSAT wide-swath coverage provide two–three sequential daily observations of common ice features at image overlaps. The sampling interval is at the orbital period of ~ 100 min; the motion field is sampled on a uniform 10-km grid. The tracking of common ice features in a sequence of SAR images is described in [Kwok et al. \(1990\)](#).

Monthly sea level pressure (SLP) are computed from the National Centers for Environmental Prediction–National Center for Atmospheric Research (NCEP–NCAR) reanalysis output ([Kalnay et al. 1996](#)) and the European Centre for Medium-Range Weather Forecasts (ECMWF) 40-yr Re-Analysis (ERA-40) fields. The monthly Southern Oscillation indices (SOI) used in this study are those of the Climate Analysis Center. The SOI is the difference between the standardized Tahiti SLP and the standardized Darwin SLP measurements. Large negative excursions of the SOI are associated with intense El Niño–Southern Oscillation (ENSO) episodes. The indices of the Southern Hemisphere annular mode (SAM; [Thompson and Wallace 2000](#)) are coefficients of the leading mode in the EOF expansion of the 850-hPa geopotential height fields poleward of 20°S from the NCEP–NCAR (N–N) reanalysis. This mode explains over 30% of the variance of the monthly mean fields. The SAM describes a predominantly zonally symmetric pattern and is characterized by seesaws of atmospheric mass between the polar cap regions poleward of 60°S and the surrounding zonal ring centered along $\sim 45^\circ\text{S}$. This annular mode is related to strong perturbations in temperature and total ozone column over the polar caps during the stratosphere’s active season, and enhanced westerlies north of 70°S during the positive phases of this index.

b. Quality of PMW ice motion of the Ross Sea

Comparisons between the two motion datasets are performed across and along the flux gate shown in [Fig. 1](#) . The eastern and western termini of the gate, with lengths of ~ 1400 km, are located at Land Bay and Cape Adare. We refer to the enclosed area ($\sim 490 \times 10^3 \text{ km}^2$) as the Ross Sea. The positional errors in the SAR estimates (~ 300 m; [Lindsay](#)

[and Stern 2003](#)) used here are significantly smaller than the uncertainties in the PMW motion (on the order of kilometers) and thus are considered as truth in the following analysis. As the sampling of the SAR ice motion is not uniform in time and space, the first step in this process is to construct equivalent PMW displacements at coincident times and locations as that of RADARSAT ice motion measurements. At a given location, the gridded daily 85-GHz PMW ice motion is spatially and temporally interpolated to provide fractional-day displacements and summed to obtain the net displacements with equal time separations as that of the SAR ice motion observations.

[Figure 2](#) shows the comparison of the two components of the motion vector and the monthly distribution of SAR motion measurements during 1998 and 2000. No motion estimates are in June or July because RADARSAT imagery was not acquired due to spacecraft power constraints during these months of the austral winter. During the two years, the correlations between the 85-GHz and SAR ice motion at the flux gate are reasonable ($0.77 < \rho < 0.88$). The biases are small, the standard deviations of the differences in the vector components range between 4.3 and 5.3 km day⁻¹, and the directional differences are $-0.3^\circ \pm 32^\circ$ and $5.5^\circ \pm 37^\circ$. These results are comparable to our assessment of PMW/RADARSAT ice motion (with an uncertainty of ~ 4.5 km day⁻¹) at the Fram Strait ([Kwok et al. 2004](#)) and show relative consistency in the quality of derived PMW motion estimates.

3. Large-scale ice motion

a. General circulation pattern

[Figure 3](#) shows the mean monthly circulation of sea ice within a broad region including the Ross Sea from 12 yr of PMW ice motion. The cyclonic pattern associated with the synoptic-scale low, centered over the northeast Ross Sea, dominates the mean ice circulation over all months between April and November. The pattern is characterized by an inflow of sea ice into the Ross Sea from the east, along the coast of the embayment, in contrast to a considerably stronger northwestward outflow in the west. This can be seen in the velocity profiles at the flux gate ([Figs. 4](#) and [5](#)). This imbalance in the overall circulation points to significant divergence and production of open water and ice areas in polynyas off the Ross Ice Shelf that seems to be a persistent phenomenon during all winter months. Some recirculation of the outflow in the eastern Ross Sea is also evident. North of Cape Adare, the ice splits into two branches with one moving westward and the other northward. Farther north, the prevailing motion is toward the east as the ice becomes entrained in the Antarctic Circumpolar Current.

Atmospheric forcing plays a significant role in the enhancement of the sea ice outflow in the western Ross Sea. This is related to ice area production at polynya events at the ice front of the Ross Ice Shelf (the Ross Sea polynya, sometimes referred to as the Ross Ice Shelf polynya) and Terra Nova Bay (the Terra Nova Bay polynya). Data from automatic weather stations (AWS) deployed over the Ross Ice Shelf reveal that the dominant

surface airflow over the western Ross Ice Shelf is northward, passes to the east of Ross Island ([Savage and Stearns 1985](#)) and appears to be the primary atmospheric forcing for development of the Ross Sea polynya ([Bromwich et al. 1993](#)). [Bromwich et al. \(1998\)](#) find that synoptic cyclones near Roosevelt Island induce SLP distributions over the Ross Ice Shelf with isobars oriented parallel to the Transantarctic Mountains. This setup results in an intensification and northward propagation of the katabatic winds across the ice shelf with an associated low-level warming. An immediate impact of katabatic surges is the development of polynyas where heat and salt fluxes associated with new ice growth are intense: about 60% of the polynya events are linked to katabatic surge events; 40% from katabatic drainage winds (from glaciers); and barrier winds (winds that flow northward along the Transantarctic Mountains and deflected eastward by topographic barriers along the Scott coast; [Bromwich et al. 1998](#)).

b. Response to geostrophic wind

With RADARSAT ice motion, we examine the linear relationship between the ice velocity u , the geostrophic wind G , and the mean ocean current c , of the form $u = AG + c + \mathcal{E}$ used by [Thorndike and Colony \(1982\)](#). Here A is a complex coefficient where the magnitude $|A|$ is typically referred to as the scaling factor between the speed of the wind and ice, and an angle θ representing the turning of the ice to the left (+) or right (−) of the wind. Here \mathcal{E} represents that part of the ice velocity that is neither a constant nor a linear function of the wind.

[Table 1](#) summarizes the monthly estimates of $|A|$ and θ and the squared correlation, ρ^2 , of the coefficient made with the available data in 1998. The geostrophic wind field ($\mathbf{G} = -(\mathbf{k}/f\rho) \times \nabla P$; f = Coriolis parameter; ρ = air density; P = sea level pressure; and \mathbf{k} is the surface normal) is derived from the NCEP–NCAR surface pressure fields. We note that the correlations are between two estimated quantities and errors in these quantities are somewhat lower than the true correlations. Using only observations that are more than 300 km from the coast, analysis shows that the ice moves with a speed of $\sim 1.7\%$ of the wind, and $\sim 4^\circ$ to the left of the geostrophic wind. The squared correlations vary between 0.4 and 0.76. At distances of less than 300 km, ρ^2 (not shown here) is generally much lower implying the presence of other physical effects close to the coast that weaken this relationship between the ice velocity and geostrophic wind. In the Arctic Ocean the effect of the coastline is felt within about 400 km from the coast ([Thorndike and Colony 1982](#)). These results can be compared to that obtained in the Weddell Sea ([Kottmeier and Sellmann 1996](#)) and the Arctic Ocean ([Thorndike and Colony 1982](#)). In the Weddell Sea, $|A|$ increases from 0.5% ($\rho^2 = 0.5$) in the southwestern to $\sim 1.5\%$ ($\rho^2 = 0.8$) in the northern, central, and eastern Weddell Sea. In contrast, $|A|$ varies between $\sim 1\%$ in the summer and $\sim 0.8\%$ in the winter ($\rho^2 = 0.7$) over the Arctic ice cover. The similarity between the magnitude of A in the northern, central, and eastern Weddell Sea and the Ross Sea suggests comparable ice conditions, with a divergent seasonal ice cover of relatively thin ice, lower ice concentration (lower internal ice stress) and perhaps comparable structure of the atmospheric boundary layer. We did not examine the ocean current, c , or investigate the local variability of A because of this rather small dataset.

4. Ice area flux from PMW ice motion (1992–2003)

The daily area flux, F , is estimated by integrating the cross-gate motion profile using the simple trapezoidal rule, $F = \sum_{i=1}^{n-1} 0.5(u_i + u_{i+1})C_i\Delta x$, where u is the magnitude of the motion perpendicular to the flux gate, Δx is the spacing between the motion estimates, C_i is the ice concentration (between u_i and u_{i+1}) from PMW analyses, and n is the number of motion samples along the gate.

a. Cross-gate motion profile

Following the procedure in [Kwok and Rothrock \(1999\)](#), cross-gate motion profiles are created by interpolating the gridded PMW ice motion to 50 uniformly spaced points (~ 28 km separation) along the ~ 1400 km flux gate. Cubic splines, constrained to go to zero at the endpoints, are fitted to the two components of the motion vectors to fill gaps in the motion estimates along the gate. This boundary condition is necessary as there are rarely motion estimates near the coast; the implication of this assumption is discussed in the next section. The vectors are then projected onto the unit normal of the flux gate to obtain the magnitude of ice motion through the gate. [Figure 4](#) shows comparisons of the gate-perpendicular (\perp) and gate-parallel (\parallel) profiles of the 85-GHz PMW estimates with available RADARSAT-derived ice motion. In addition to the quantitative comparison shown in [section 2](#), the broad agreements in the magnitude and shape of cross-gate velocity profiles indicate the motion estimates are of reasonable quality.

[Figure 5](#) shows the average and variability of the monthly profiles from the 12 yr. As discussed earlier, the gate-perpendicular profile shows the largest outflow in the western part of the gate; the peak of the profile centered slightly east of 180° . Along the gate, the predominant westward advection of ice can be seen in the gate-parallel (\parallel) profile with a peak even more skewed toward the western Ross Sea. It is also notable that the magnitudes of the gate-parallel and gate-perpendicular profiles are comparable. The gate-perpendicular profile (inflow) is generally smaller in the east and the parallel profile shows a dominant mean westward motion.



b. Area flux estimates from PMW ice motion

First we consider the dependence of the uncertainties in the flux estimates on errors in the PMW ice motion. Taking into account the patch sizes (~ 90 km by 90 km) used in the ice tracking, there are ~ 16 independent 85-GHz ice motion observations along the flux gate. Following the analysis in [Kwok and Rothrock \(1999\)](#), if we assume that the errors of the motion samples are additive, unbiased, uncorrelated, and normally distributed, the uncertainties in the daily area flux estimates, σ_F , are given by $\sigma_F(\text{km}) = (\sigma_u/(N_s)^{1/2})L$, where L is the length of the flux line (approximately 1400 km), σ_u is the standard error in the motion estimates, and N_s is the number of independent samples. For $N_s = 16$ and $\sigma_u = 5$ km, the uncertainty in the daily 85-GHz area flux is approximately 1750 km^2 compared

to the average daily flux of 3700 km^2 . This shows that on a daily basis, the estimates are rather noisy.

The uncertainty in the average winter (March–November) area flux estimates, σ_T , again assuming that the errors of the area flux are additive, unbiased, uncorrelated, and normally distributed is $\sigma_T(\text{km}) = \sigma_F(N_D)^{1/2}$. Here N_D is the number of observations over the winter and σ_F^2 is the sum of N_D random variables with variance σ_F^2 . We do not expect these errors to be correlated since individual area flux estimates are derived from temporally distinct PMW fields. There are ~ 270 daily flux estimates between March and November. This results in uncertainties in the winter area flux, σ_T , of approximately $30 \times 10^3 \text{ km}^2$ for the daily 85-GHz observations. This is less than 3% of the average annual winter area flux of about $990 \times 10^3 \text{ km}^2$.

A second source of error in the area flux estimates is the model of the motion profile near the coast. We assume that there is no motion at the coastal endpoints of the flux gate and that the motion increases smoothly from those points to 35 km off the coast where the observations are available. A departure from this assumption would introduce biases in the area flux estimates. In the worst case, if the profiles were uniform across the gate and the motion near the coasts did not go to zero, we would underestimate the area flux by approximately 10%.

The winter area flux is the total of the daily 85-GHz area flux from the beginning of March until the end of November. [Figure 6](#)  summarizes the record of winter area flux at the gate. The average area flux over this period is $990 \times 10^3 \text{ km}^2$ and ranges from a minimum of $600 \times 10^3 \text{ km}^2$ in 1992 to a peak of $1600 \times 10^3 \text{ km}^2$ in 2001—an almost threefold variability. The Ross Sea within the flux gate, covering an area of $\sim 490 \times 10^3 \text{ km}^2$, exports more than twice its own area of sea ice every 9 months. The standard deviation in the winter flux, at $300 \times 10^3 \text{ km}^2$, is high. A positive trend of $\sim 30 \times 10^3 \text{ km}^2 \text{ winter}^{-1}$ can be seen in the record; however, the caveats in attributing significance to the trend of a short record apply. Seasonally, the mean monthly plot ([Fig. 6a](#) ) shows that the ice flux is generally smaller in March and November.

The area flux estimates represent the net area flux, that is, $\text{net} = \text{export} - \text{import}$. The net would be ice area that is produced in the Ross Sea if there were no melt or deformation of the sea ice advected into the area; the net production would be zero if export equals import. Thus, it is interesting to examine the two contributions to the net because it provides a rough estimate of the ice that is advected in from the east and the total exported in the west (i.e., the ice area produced in the Ross Sea and the re-export of the eastern inflow). The average area exported over this period is $1390 \times 10^3 \text{ km}^2$ and the average area imported over this period is $470 \times 10^3 \text{ km}^2$. The net positive trend during the 12 yr appears to be a result of a positive trend in the total export and a smaller negative trend in the area inflow.

5. Connections to atmospheric forcing

In this section, the relations of area flux to cross-gate pressure gradient and larger-scale atmospheric modes are explored. At the outset, we recognize that the representation of the Southern Hemisphere high latitude in atmospheric reanalysis products may not be ideal for investigation of variability and trends at synoptic time scales. [Bromwich and Fogt \(2004\)](#) find that the ERA-40 fields seem to be more strongly constrained by satellite data compared to N–N and differences in assimilation schemes can lead to large discrepancies in the products. In particular, some of the issues (e.g., spurious trends and jumps, etc.) with the N–N analyses have been highlighted in [Hines et al. \(2000\)](#) and [Marshall \(2003\)](#). Our approach is to 1) examine these connections in the context of both the N–N and ERA-40 reanalyses; and 2) restrict our attention to the period between 1979 and 2001 when better-quality and higher quantities of observational data are available for assimilation into the reanalysis schemes. Agreements and disagreements will be discussed with the recognition that consistency increases, to some extent, the confidence in the observed associations. Differences can also point to the relative deficiencies of these meteorological fields.

a. Relation to cross-gate pressure gradient

First, we examine the correlation between the winter area flux and the gradient in the SLP across the flux gate (i.e., the difference between the SLP at the west and east endpoints) during the 12 yr. This gradient provides a measure of the strength of the cyclonic circulation because the gate cuts across the dominant low in SLP over the Ross Sea. [Table 2](#) and [Fig. 6](#) show this correlation during the winter (March–November). With ice motion that is largely wind driven, the dependence of the area flux on the SLP gradient (ΔP) is expected to be reasonably high. Indeed, between 1992 and 2003 the gradient (an average of ~ 7 hPa: N–N) explains more than 61% of the variance in the ice area flux; and for the shorter duration (1992–2001) ERA40 fields, $\sim 59\%$. Unexplained variance could be due to many factors including uncertainty in the two quantities and perhaps, though not exclusively, the effects of unmodeled katabatic wind and mesoscale cyclones.

Since ΔP and area flux are highly correlated, we can use this to examine the historical record of area flux when ice motion measurements are not available. One question is whether there is a long-term trend in ΔP . Similar to the uptrend in the 12-yr area flux record, we find positive trends in the winter ΔP in both the N–N and ERA-40 results. These trends are also positive in the longer record between 1979 and 2001; the N–N fields give a higher winter (March–November) trend of $1.7 \text{ hPa decade}^{-1}$ compared to the $0.3 \text{ hPa decade}^{-1}$ in the ERA-40 analysis. When the summer months are included ([Fig. 7a](#)) the ERA-40 gives a small negative trend. The two records (1979–2001) of anomalies in monthly cross-gate pressure gradient, however, are only correlated at 0.6. An appreciable jump in ΔP in 1998 is evident in the N–N fields compared to that from ERA-40. Whether this is an artifact is not clear but it is interesting to note that the area flux, an entirely independent estimate, is better correlated in terms of trend and variability to the ΔP (N–N) over the 12 yr.

Over this same period, negative trends in the anomalies in monthly SLP (N–N: -1.8 hPa decade⁻¹; ERA-40: -0.9 hPa decade⁻¹) are seen in both records. This regional mean is computed over the open-ocean and sea ice areas within the boundaries of [Fig. 1](#). [Hines et al. \(2000\)](#) noted that a stronger winter trend in N–N versus ERA-40 is expected as the circumpolar trough anomalously deepens in N–N into the 1990s. Whether these declines in SLP reflect realistic climate changes or are due to artifacts in reanalysis results are not clear. In contrast to ΔP , these anomalies are correlated at 0.95. Perhaps this is not surprising as the regional mean pressure may be better represented in the reanalysis products compared to gradients between two points. Nevertheless, a correlation of 0.6 seems low. It is also interesting to point out that the patterns in the trend in SLP anomalies over the circumpolar Southern Ocean computed from the N–N and ERA-40 fields are similar ([Fig. 7](#)) but the spatial variability is higher in the N–N fields.

b. Connections to the Southern Oscillation and Southern Hemisphere annular mode

The next question is one of attribution: Is ΔP associated with local expressions of large-scale atmospheric modes [e.g., Southern Oscillation (SO) and SAM]? An established link of area flux, a local process in the Ross Sea, to larger-scale atmospheric circulation patterns would be interesting for understanding its connection to polar and extrapolar climate. Over the rather short 12-yr period, the squared correlations between the area flux and the SOI and the SAM index (SAMI) are moderate at 0.3 and 0.44. Squared correlations between ΔP computed from N–N/ERA-40 fields and SOI are 0.46 and 0.44, respectively. Similarly, between ΔP and SAMI the correlations are 0.25 and 0.14, respectively. This is not surprising as the extratropical center of action of the SO is located toward the Bellingshausen and Amundsen Seas away from the Ross Sea ([Kwok and Comiso 2002](#)) and the SAM encompasses near-hemispheric surface pressure variability from 20° to 90°S.

These positive correlations indicate that increased area flux and ΔP are associated with positive excursions of these atmospheric indices. To explore these connections, we examine the differences in the monthly SLP anomalies in the Ross Sea associated with the positive and negative polarities of the SOI and the SAMI by averaging the anomaly fields that fall within three ranges of the two indices. These spatial composites allow us to examine the dominant spatial pattern of the SLP anomalies associated with the extreme behavior of the two atmospheric modes. The three phases that we select are not symmetric about zero (SOI > 0, $0 \geq \text{SOI} \geq -1$, and SOI < -1). The rationale for this division is that the mean of the SOI is nonzero and has a significant negative bias. These ranges give us an approximately equal number of anomaly fields in the positive (SOI⁺), neutral (SOI⁰), and negative (SOI⁻) phases, respectively. The composite fields for three different phases of the SAM (SAMI > 0.8, $0.8 \geq \text{SAMI} \geq -0.3$, SAMI < -0.3) are constructed similarly. [Figure 8](#) shows the differences in the spatial distribution of SLP anomalies between the positive and negative phases of the two indices in the Ross Sea and along the gate. These differences highlight the contrast under those conditions.

The SOI analysis, in both the N–N and ERA-40 fields, shows that there is an increased SLP gradient (higher SLP in the west compared to the east) along the gate during the

positive phases of SOI. The N–N results show a slightly higher gradient. We attribute this spatial pattern to the extratropical center of action of the SO. The SO has a signature that clearly extends to the mid- and polar latitudes of the Southern Hemisphere ([Kwok and Comiso 2002](#)). South of 50°S, two distinct spatial patterns of SLP are associated with the two extreme phases of SOI. In the SOI⁺ SLP composite ([Fig. 1](#); [Kwok and Comiso 2002](#)), a zone of negative SLP anomaly is located off the Antarctic coast in the Amundsen and Bellingshausen Seas; this zone of SLP anomalies extends to the Ross Sea. An anomaly pattern of opposite polarity can be found in the SOI[−] SLP composite. It seems that the higher cross-gate SLP gradient during the positive phase is associated with these SLP anomalies at the periphery of this spatial center of action of the SO.

Similarly, the SAM results show an increased SLP gradient along the gate during its positive phases. This increase is more moderate as evidenced by the lower correlation between ΔP and SAMI. Spatially, the most striking polar features associated with the positive polarity of the SAMI are the negative SLP anomalies within the circumpolar trough, enhancement of the westerlies north of 70°S, and negative anomalies in the meridional wind west of the Antarctic peninsula. The negative differences are due to generally lower SLP during the positive phase of SAM. It appears that this enhancement in ΔP is a local expression of the SLP distribution during the positive phase of the SAM.

The above analyses paint a broad picture of the linkages to two atmospheric modes. Beyond the satellite era if the linkages are robust, these could be used as proxy indicators of ice export: an important aspect of the overall Ross Sea ice behavior. The physical mechanisms associated with the atmospheric variability indicated here are complex and beyond the scope of the discussion. However, the identified relationships are useful as diagnostic tools for climate models and for the eventual understanding of the underlying mechanisms of these associations.

6. Ice deformation: Small scale

For the Ross Sea, the characteristics of small-scale ice motion and deformation have not been previously investigated. Off the ice front and away from the polynyas, small-scale deformation is dependent on wind forcing and at short temporal scales on strong tidal and inertial forcing. Quantifying this deformation is essential for understanding its contribution to the regional brine flux and ice production. Here, we examine this deformation rates derived from ice motion sampled on a grid 10 km on a side. From the motion fields, the divergence, and shear of each grid cell are computed via $\nabla \cdot u = u_x + v_y$, $e = [(u_x - v_y)^2 + (u_y + v_x)^2]^{(1/2)}$. Here u_x , u_y , v_x , and v_y are the spatial gradients in ice motion computed using a line integral around the boundary of each cell (≈ 10 km on a side). The line segments connecting the four vertices of a cell define the boundaries. Here $\nabla \cdot u$ is a measure of area change, and e is the scalar magnitude of shear.

a. Daily deformation

Over the two years, there are a total of 120 daily motion and deformation fields derived from the RADARSAT imagery. There are spatial gaps in the coverage of the Ross Sea and full coverage is dependent on orbit geometry and image availability. However, the daily coverage is generally good. The seasonal distribution of these observations is shown in [Fig. 2a](#). [Figure 9](#) shows four examples. Isobars of average SLP are superimposed on the motion fields. Geostrophic wind direction is parallel to the contour lines. To first order, ice motion is to the left but near parallel to the wind. To second order, there are small velocity differences between quasi-rigid ice floes that give rise to fractures that are evident in the deformation fields.

Several common features can be pointed out in the results. The deformation rates are typically largest near the ice shelf front. This can be seen in the deformation fields as well as in the plot ([Fig. 10](#)) showing the dependence of divergence on distance from coastline or ice front. In the mean, the ice cover is net divergent within 100 km but decreases rather quickly even though the variability remains high. Deformation is localized along fractures zones; there are large areas with little or no deformation. Katabatic winds from the ice shelf or drainage from glaciers push the ice cover northward away from the coast to create large areas of open water—the Ross Sea and Terra Nova Bay polynyas. [Figure 11](#) shows two RADARSAT images of active Ross Sea polynyas. The open-water/thin ice areas and the ice edge just north of the ice shelf are very distinctive and have higher backscatter due to wind roughening. The Langmuir-generated bright linear streaks seen here are characteristic of polynyas ([Drucker et al. 2003](#)). Another feature in the motion field that is not captured in the larger-scale motion or surface pressure fields is the eastward ice motion due to the drainage winds from the glaciers along the Scott coast. This pattern, present in three of the four examples, shows an area of large deformation east of McMurdo Sound associated with convergence of the eastward flow with the northward drift away from the Ross Ice Shelf. Ice motion in the Ross Sea embayment is predominantly to the northwest, but in the inner embayment over the continental shelf, it is opposed by ice being pushed offshore by wind from the Scott coast/southern Victoria Land. The separation between the two regimes of ice motion stands out in the SAR imagery as well as the deformation fields. [Sturman and Anderson \(1986\)](#) also observed this as an area of convergence and it explains the more extensive ridging observed in this region ([Weeks et al. 1989](#)).

b. Subdaily motion and deformation: Variability

Short-period ice motion and deformation estimates are derived from sequential RADARSAT imagery. The high-frequency repeat imaging of a region of the ice cover takes advantage of the coverage overlap afforded by the RADARSAT wide-swath (460 km) SAR mode and the convergence of the satellite ground tracks at high polar latitudes. Near $\sim 75^\circ\text{S}$, the westward precession of the orbit track provides two–three sequential image observations every day with a sampling interval at the orbital period of ~ 100 min, for a maximum of two motion fields every day. This restricts our examination to short-period variability in motion and deformation rather than the more interesting oscillatory behavior at daily or semidiurnal periods associated with inertial or tidal cycles. Also, because of the intermittent record, we cannot separate the longer-period divergent and

convergent events associated with wind forcing superimposed on the shorter-scale periodic behavior seen in the two time series.

The results from the total of 34 subdaily fields of ice motion, with sampling intervals of one and two orbital periods, are summarized in [Table 3](#). Areal coverage of each field ranges from $16 \times 10^3 \text{ km}^2$ (160 grid cells) to $82 \times 10^3 \text{ km}^2$ (820 grid cells). All of the sampled areas are located in the Ross Sea region. Divergence/convergence rates vary between $5.9 \times 10^{-7} \text{ s}^{-1}$ and $-5 \times 10^{-7} \text{ s}^{-1}$, which translate into fractional area changes of between 5.1% and $-4.3\% \text{ day}^{-1}$. This is ~ 5 times larger than the rates observed within the Arctic Ocean ice cover of $\sim 10^{-7} \text{ s}^{-1}$ ([Kwok et al. 2003](#)). The ice velocity is also remarkable with a maximum of more than 60 cm s^{-1} seen in our dataset. The importance of subdaily ice motion and deformation in ice production and brine flux is not known; the relative contribution of this process to ice production within the ice cover compared to that in the polynyas is an important question.

7. Conclusions

The sea ice motion, area flux, and deformation of the Ross Sea ice cover are examined with PMW and available RADARSAT ice motion. Over the 12 yr, analyses show a dominant cyclonic circulation pattern over all winter months between March and November. In response to geostrophic wind, the ice in the Ross Sea moves at $\sim 1.7\%$ of the wind, comparable to that observed in the northern and eastern Weddell Sea. Between 1992 and 2003, a significant positive trend ($\sim 30 \times 10^3 \text{ km}^2 \text{ yr}^{-1}$) can be seen in the winter area flux that has a mean of $990 \times 10^3 \text{ km}^2$ and ranges from low of $600 \times 10^3 \text{ km}^2$ in 1992 to a peak of $1600 \times 10^3 \text{ km}^2$ in 2001.

Taking the typical ice thickness at the gate to be that observed by [Jeffries and Adolphs \(1997\)](#) during one cruise in 1995 (i.e., 0.5 m) a rough estimate of the ice production rate gives a range of $300\text{--}800 \text{ km}^3$ or $\sim 0.6\text{--}1.6 \text{ m winter}^{-1}$ within the $490\,000 \text{ km}^2$ area inside the gate. Even though the variability is quite high, this is less than that estimated by [Jacobs et al. \(2002\)](#) of $\sim 2.5 \text{ m}$; this discrepancy is probably due to different assumptions used in computing the estimate. Lacking coincident ice thickness estimates makes it difficult to assess the mean, variability, and much less the trend in ice production. Ice growth depends on small differences between the atmospheric and oceanic heat balance at the surface. Offshore winds increase divergence of the ice cover but katabatic wind surges, responsible for about 60% of polynya events ([Bromwich et al. 1998](#)) are also associated with low-level warming: this slows ice growth. So the conditions related to increased area production may not be conducive to increased ice growth or volume production. Polynya formation may also be influenced by oceanic sensible heat, as hydrographic investigations have shown a strong upwelling of warm deep water onto the continental shelf in front of the ice shelf ([Pillsbury and Jacobs 1985](#)). These and other factors that can influence ice area and volume production underscore the importance of thickness measurements well distributed in space and time for understanding local processes and trends. At this writing, the use of radar or laser altimeters ([Laxon et al.](#)

[2003](#) ; [Kwok et al. 2004](#)) for estimation of thickness of Southern Ocean sea ice remains to be demonstrated.

The cross-gate gradient in SLP explains ~60% of the variance in area export. If this correlation is indeed robust over longer time scales, we can examine past area export by compiling this record in longer-term atmospheric reanalyses. Over the 12 yr, the trends in ΔP in the N–N and ERA-40 reanalyses are both positive. Between 1979 and 2001, the winter trends are positive, but when the summer months are included, results from the reanalysis products do not agree and are of opposite polarity. The correlation between the monthly anomalies in SLP gradient time series is only 0.6 but is 0.94 between the monthly anomalies in mean SLP over the Ross Sea region. While both products suggest a negative trend in SLP anomalies, several investigators have advised caution in the use of these datasets for examining synoptic time scales processes in high southern latitudes because of the possibility of jumps and spurious trends. A positive trend in ΔP (deeper low) might support one scheme (proposed by [Jacobs et al. 2002](#)) of how a “spinup” of the polar gyre could account for the salinity decline in the Ross Sea: the strengthened circulation would increase the intrusion of warm deep water into the continental shelf and increase the basal melting of the ice shelf while decreasing sea ice production.

At shorter time scales, we explore the linkage of the monthly variability of ΔP to the SO and SAM by examining their spatial expressions in the Ross Sea region. In this case, both the N–N and ERA-40 anomalies agree. Distinct increases in the ΔP associated with the positive phases of the SO and SAM can be seen in the anomaly composites in both N–N and ERA-40 reanalyses. For the SO, the SLP anomalies in the Ross Sea are associated with the center of action in the Amundsen/Bellingshausen Seas; for the SAM, this is associated with a local spatial pattern in the vicinity of the Ross Sea. In the mean, it would indicate that ΔP would be enhanced when both SO and SAM are in their positive phases. Indeed, the sum of the two indices explains more of the variance of the ΔP : 55%/49% compared to the 46%/44% (N–N/ERA-40) and 25%/15% for SOI and SAMI alone. The relationship between the SAM and SO indices is weak; the two indices are correlated at 0.1 over the 22 yr. It would appear that there could be a linear coupling of the two atmospheric modes. The SAM indices have trended toward more positive values while the SO indices have drifted toward more negative values since the beginning of the period. These local expressions of the in-phase and out-of-phase behavior of the two modes and their effect on Antarctic processes is worth further investigation. Recent work of Fogt and Bromwich (2005, manuscript submitted to *J. Climate*) indicate that the coupling in the SO and SAM indices between the 1980s and 1990s seems to be seasonal and confined to the austral spring, but the quality of the reanalysis products limited the length of this study.

The small-scale ice motion from high-resolution SAR imagery provides a glimpse of the variability of the deformation at daily and subdaily time scales. As expected, divergence is highest just north of the ice shelf where the values can reach 1.0 day^{-1} . This variability drops quickly to 0.1 day^{-1} within 100 km of the ice shelf. In the mean, the ice cover is net divergent even when the divergence near the ice front is ignored. Variability of subdaily ice motion and deformation are also high. In subdaily observations near the

edge of the Ross Sea polynya, we have seen ice velocities $> 60 \text{ cm s}^{-1}$ and convergence of 0.4 day^{-1} in several areas in April 2000. Subdaily ice deformation in the Ross Sea, in response to tidal and inertial forcing, has the potential of producing a significant fraction of sea ice and brine flux, but these need to be quantified.

In summary, this present examination provides a view of the variability Ross Sea ice cover with available ice motion datasets. Passive microwave ice motion adds to the available datasets that offer systematic observations of the Ross Sea. Small-scale ice motion from SAR imagery, albeit limited at this time, has the potential of providing high-resolution observations of the behavior of the ice cover at short temporal and spatial scales. Ice motion, together with better measurements of other characteristics of the ice cover (e.g., ice/snow thickness) are crucial for understanding its long-term behavior and interactions with the polar and global climate.

Acknowledgments. I wish to thank Stan Jacobs and Seelye Martin for their valuable suggestions and careful reading of this manuscript, and S. S. Pang for her software support during the course of this study. The RADARSAT image data are provided by the Alaska Satellite Facility, Fairbanks, Alaska. The SMMR and SSM/I brightness temperature and ice concentration fields are provided by World Data Center A for Glaciology/National Snow and Ice Data Center, University of Colorado, Boulder, Colorado. This work was carried out at the Jet Propulsion Laboratory, California Institute of Technology, under contract with the National Aeronautics and Space Administration.

REFERENCES

- Agnew, L., H. Le, and T. Hirose, 1997: Estimation of large scale sea ice motion from SSM/I 85.5 GHz imagery. *Ann. Glaciol.*, **25**, 305–311.
- Broecker, W. S., and Coauthors, 1998: How much deep water is formed in the Southern Ocean?. *J. Geophys. Res.*, **103**, C8, 15833–15843.
- Bromwich, D. H., and R. L. Fogt, 2004: Strong trends in the skill of the ERA-40 and NCEP–NCAR reanalyses in the high and middle latitudes of the Southern Hemisphere, 1958–2001. *J. Climate.*, **17**, 4603–4619.
- Bromwich, D. H., J. F. Carrasco, Z. Liu, and R.-Y. Tseng, 1993: Hemispheric atmospheric variations and oceanographic impacts associated with katabatic surges across the Ross Ice Shelf, Antarctica. *J. Geophys. Res.*, **98**, 13045–13062.
- Bromwich, D. H., Z. Liu, A. N. Rogers, and M. L. van Woert, 1998: Winter atmospheric forcing of the Ross Sea Polynya. *Ocean, Ice, and Atmosphere: Interactions at the Antarctic Continental Margins*, S. S. Jacobs and R. F. Weiss, Eds., AGU Antarctic Research Series, Vol. 75, Amer. Geophys. Res., 101–133.
- Cavalieri, D. J., 1992: The validation of geophysical products using multisensor data. *Microwave Remote Sensing of Sea Ice*, F. D. Carsey, Ed., Amer. Geophys. Union, 233–

Drucker, R. D., S. Martin, and R. Moritz, 2003: Observations of ice thickness and frazil ice in the St. Lawrence Island polynya from satellite imagery, upward looking sonar, and salinity/temperature moorings. *J. Geophys. Res.*, **108**, 3149, doi:10.1029/2001JC001213.

Foster, T. D., and E. Carmack, 1976: Temperature and salinity structure in the Weddell Sea. *J. Phys. Oceanogr.*, **6**, 36–44.

Gloersen, P., W. J. Campbell, D. J. Cavalieri, J. C. Comiso, C. L. Parkinson, and H. J. Zwally, 1992: Arctic and Antarctic sea ice, 1978–1987: Satellite passive-microwave observations and analysis. NASA Special Publ. 511, 290 pp.

Gordon, A. L., 1991: Two stable modes of Southern Ocean winter stratification. *Deep Convection and Deep Water Formation in the Oceans*, P. C. Chu and J. C. Gascard, Eds., Elsevier Oceanographic Series, Vol. 57, Elsevier, 17–35.

Goosse, H., and T. Fichefet, 1999: Importance of ice-ocean interactions for global ocean circulation: A model study. *J. Geophys. Res.*, **104**, C10, 23337–23355.

Hines, K. M., D. H. Bromwich, and G. J. Marshall, 2000: Artificial surface pressure trends in the NCEP–NCAR reanalysis over the Southern Ocean and Antarctica. *J. Climate.*, **13**, 3940–3952.

Jacobs, S. S., and J. C. Comiso, 1989: Sea ice and oceanic processes on the Ross Sea Continental Shelf. *J. Geophys. Res.*, **94**, C12, 18195–18211.

Jacobs, S. S., C. F. Giulivi, and P. A. Mele, 2002: Freshening of the Ross Sea during the late 20th century. *Science.*, **297**, 386–389.

Jeffries, M. O., and W. F. Weeks, 1992: Structural characteristics and development of sea ice in the Western Ross Sea. *Antarct. Sci.*, **5**, 63–75.

Jeffries, M. O., and U. Adolphs, 1997: Early winter ice and snow thickness distribution, ice structure and development of the western Ross Sea pack ice between the ice edge and the Ross Ice Shelf. *Antarct. Sci.*, **9**, 188–200.

Jeffries, M. O., R. A. Shaw, K. Morris, A. L. Veazey, and H. R. Krouse, 1994: Crystal structure, stable isotopes, in the Ross, Amundsen, and Bellingshausen seas, Antarctica. *J. Geophys. Res.*, **99**, 985–995.

Kalnay, E., and Coauthors, 1996: The NCEP/NCAR 40-Year Reanalysis Project. *Bull. Amer. Meteor. Soc.*, **77**, 437–471.

Kottmeier, C., and L. Sellmann, 1996: Atmospheric and oceanic forcing of Weddell Sea ice motion. *J. Geophys. Res.*, **101**, C9, 20809–20824.

- Kwok, R., and D. A. Rothrock, 1999: Variability of Fram Strait ice flux and North Atlantic Oscillation. *J. Geophys. Res.*, **104**, C3, 5177–5189.
- Kwok, R., and J. C. Comiso, 2002: Southern Ocean climate and sea ice anomalies associated with the Southern Oscillations. *J. Climate.*, **15**, 487–501.
- Kwok, R., J. C. Curlander, R. McConnell, and S. Pang, 1990: An ice motion tracking system at the Alaska SAR facility. *IEEE J. Oceanic Eng.*, **15**, 44–54.
- Kwok, R., A. Schweiger, D. A. Rothrock, S. Pang, and C. Kottmeier, 1998: Sea ice motion from satellite passive microwave imagery assessed with ERS SAR and buoy motions. *J. Geophys. Res.*, **103**, C4, 8191–8214.
- Kwok, R., G. F. Cunningham, and W. D. Hibler, 2003: Sub-daily sea ice motion and deformation from RADARSAT observations. *Geophys. Res. Lett.*, **30**, 2218, doi:10.1029/2003GL018723.
- Kwok, R., G. F. Cunningham, and S. S. Pang, 2004a: Fram Strait sea ice outflow. *J. Geophys. Res.*, **109**, C01009, doi:10.1029/2003JC001785.
- Kwok, R., H. J. Zwally, and D. Yi, 2004b: ICESat observations of Arctic sea ice: A first look. *Geophys. Res. Lett.*, **31**, L16401, doi:10.1029/2004GL020309.
- Laxon, S., N. Peacock, and D. Smith, 2003: High interannual variability of sea ice in the Arctic region. *Nature.*, **425**, 947–950.
- Lindsay, R. W., and H. L. Stern, 2003: The RADARSAT geophysical processor system: Quality of sea ice trajectory and deformation estimates. *J. Atmos. Oceanic Technol.*, **20**, 1333–1347.
- Liu, A., and D. J. Cavalieri, 1998: On sea ice drift from the wavelet analysis of DMSP SSM/I data. *Int. J. Remote Sens.*, **19**, 7, 1415–1423.
- Marshall, G., 2003: Trends in the Southern Hemisphere Annular Mode from observations and reanalyses. *J. Climate.*, **16**, 4134–4143.
- Moritz, R., 1988: The Ross Sea data buoy project. *Antarct. J. U.S.*, **23**, 78–80.
- Pillsbury, R. D., and S. S. Jacobs, 1985: Preliminary observations from long-term current meter moorings near the Ross Ice Shelf, Antarctica. *Oceanology of the Antarctic Continent Shelf, Antarctica*, S. S. Jacobs, Ed., Antarctic Research Series, Vol. 43, Amer. Geophys. Union, 87–107.
- Savage, M. L., and C. R. Stearns, 1985: Climate in the vicinity of Ross Island, Antarctica. *Antarct. J. U.S.*, **20**, 1–9.

- Sturman, A. P., and M. R. Anderson, 1986: On the sea-ice regime of the Ross Sea. *J. Glaciol.*, **32**, 54–59.
- Thompson, D. W. J., and J. M. Wallace, 2000: Annular modes in the extratropical circulation. Part I: Month-to-month variability. *J. Climate.*, **13**, 1000–1016.
- Thorndike, A. S., and R. Colony, 1982: Sea ice motion in response to geostrophic winds. *J. Geophys. Res.*, **87**, 5845–5852.
- Tin, T., and M. O. Jeffries, 2001: Sea-ice thickness and roughness in the Ross Sea, Antarctica. *Ann. Glaciol.*, **33**, 187–193.
- Toggweiler, J. R., and B. Samuels, 1995: Effect of sea ice salinity of Antarctic Bottom Waters. *J. Phys. Oceanogr.*, **25**, 1980–1997.
- van Woert, M. L., 1999: Wintertime dynamics of the Terra Nova Bay polynya. *J. Geophys. Res.*, **104**, C4, 7753–7769.
- Venegas, S. A., M. R. Drinkwater, and G. Shaffer, 2001: Coupled oscillations in Antarctic sea ice and atmosphere in the South Pacific sector. *Geophys. Res. Lett.*, **28**, 3301–3304.
- Weeks, W. F., S. F. Ackley, and J. Govoni, 1989: Sea ice ridging in the Ross Sea, Antarctica, as compared with sites in the Arctic. *J. Geophys. Res.*, **94**, 4984–4988.
- White, W. B., and R. G. Peterson, 1996: An Antarctic circumpolar wave in surface pressure, wind, temperature and sea ice extent. *Nature.*, **380**, 699–702.
- Yuan, X., and D. G. Martinson, 2000: Antarctic sea ice extent variability and its global connectivity. *J. Climate.*, **13**, 1697–1717.

Tables

TABLE 1. Summary of estimated scale factor and turning angle.

1998	$ A $	θ ($^{\circ}$)	ρ^2	No. of observations
Aug	0.018	9.7	0.40	12 139 (11 days)
Sep	0.014	2.8	0.63	21 761 (14 days)
Oct	0.015	0.0	0.73	19 032 (14 days)
Nov	0.02	3.2	0.76	16 668 (13 days)

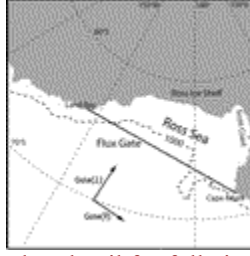
TABLE 2. Squared correlation of area flux with cross-gate pressure gradients, SOI, and SAMI (1992–2002).

ρ^2	Area flux	ΔP (NCEP)	ΔP (ERA-40)	SOI	SAMI
Area flux	1.0				
ΔP (NCEP)	0.61	1.0			
ΔP (ERA40)	0.59	0.77	1.0		
SOI	0.30	0.46	0.44	1.0	
SAMI	0.44	0.25	0.14	0.10	1.0

TABLE 3. Summary of subdaily ice motion and deformation (Uncertainty: $\approx 3 \text{ cm s}^{-1}$).

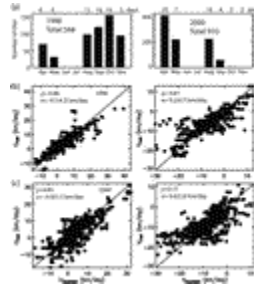
		Δt	Area	Lat	Lon	Div	Speed
	Date	(min)	(10^3 km^2)	($^\circ\text{S}$)	($^\circ\text{E}$)	(10^{-7} s^{-1})	(cm s^{-1})
1998							
Apr	20	99.3	28	75.11	177.71	1.16	3.9
	20	198.2	29	75.10	177.71	-1.85	10.9
	20	99.4	16	75.42	183.24	-0.35	3.6
	20	198.4	17	75.41	183.21	-1.50	10.8
May	2	99.2	19	75.60	192.53	4.05	7.5
	2	99.0	20	75.59	192.54	0.23	13.6
	11	198.2	32	75.11	188.19	1.97	4.6
	11	98.9	33	75.11	188.19	5.90	12.1
Aug	15	198.2	31	75.10	188.30	2.78	14.0
	15	98.9	32	75.09	188.27	1.27	20.6
	18	99.3	26	75.02	177.52	3.24	17.5
	18	198.2	27	75.00	177.46	-2.31	15.8
	30	99.2	21	75.60	192.65	1.97	25.4
	30	99.0	21	75.60	192.60	0.46	20.5
Sep	8	198.2	32	75.14	188.23	4.40	38.0
	8	98.9	33	75.13	188.15	2.55	43.8
2000							
Apr	6	99.2	70	76.00	178.63	-2.78	55.3
	6	99.2	76	75.89	178.60	-3.13	53.6
	7	99.2	82	76.32	176.71	-2.08	29.6
	7	99.4	82	76.34	176.69	-4.17	31.8
	29	99.2	29	75.91	178.82	0.81	61.9
	29	99.6	35	75.88	177.84	-1.27	63.5
	29	99.1	27	75.52	176.70	-2.66	63.4
	29	99.1	27	75.54	176.68	-4.05	67.3
	30	98.8	19	75.40	186.30	-4.98	15.6
	30	99.1	19	75.39	186.28	-4.86	22.1
May	1	99.2	81	76.32	176.91	-2.89	22.6
	1	99.4	81	76.31	176.91	-4.17	27.1
	3	99.2	30	75.70	180.89	-2.55	25.6
	3	99.1	32	75.69	180.85	-2.43	28.4
	4	99.4	74	76.24	194.47	4.63	10.6
	4	99.0	74	76.24	194.44	3.01	7.9
	9	99.1	37	75.65	175.59	-2.08	41.2
	9	99.0	35	75.62	175.59	-3.94	47.3

Figures



[Click on thumbnail for full-sized image.](#)

FIG. 1. Ross Sea flux gate, 1000-m isobath, and orientation of the gate-parallel and gate-perpendicular coordinate system. The western endpoint of the gate is located at Cape Adare and the eastern endpoint at Land Bay. The length of the gate is ~ 1400 km and the area enclosed is $\sim 490 \times 10^3$ km².



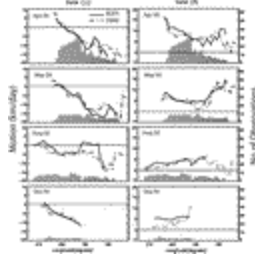
[Click on thumbnail for full-sized image.](#)

FIG. 2. Comparisons of the 85-GHz PMW and RADARSAT ice motion at the flux gate. (a) Histograms showing the distribution of RADARSAT ice motion observations in 1998 and 2000. (b) Scatterplot of the x and y components of RADARSAT and PMW ice motion (1998). (c) Scatterplot of the x and y components of ice motion (2000). The (u, v) coordinate system is aligned with that of the SSM/I polar stereographic grid where the abscissa and ordinate are along the prime and 90°E meridians, respectively. Here R is the correlation between the motion components and e is the difference between the two ice motion datasets (std dev within brackets).



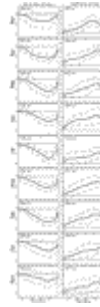
[Click on thumbnail for full-sized image.](#)

FIG. 3. Average (1992–2003) monthly ice motion fields with overlaid isobars from NN SLP fields. The Mar field is not shown here (contour intervals: 4 hPa).



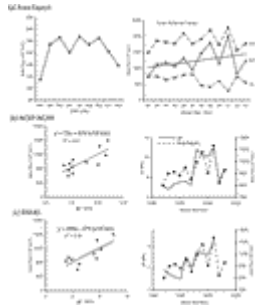
[Click on thumbnail for full-sized image.](#)

FIG. 4. Comparison of the winter 2000 85-GHz PMW and RADARSAT gate-perpendicular (\perp) and gate-parallel (\parallel) motion estimates along the gate. The solid lines show the RADARSAT motion profiles while the dashed lines show the average PMW motion profiles. The orientation of this coordinate system is shown in [Fig. 1](#). Vertical bars indicate the number of observations within each bin.



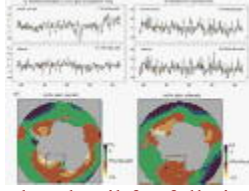
[Click on thumbnail for full-sized image.](#)

FIG. 5. Average and variability (1992–2003) of monthly gate-perpendicular (\perp) and gate-parallel (\parallel) motion profiles from 85-GHz PMW. Dash lines indicate the variability (std dev) of the motion about the mean.



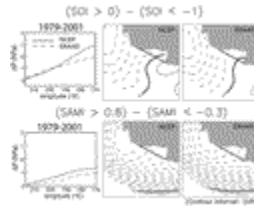
[Click on thumbnail for full-sized image.](#)

FIG. 6. Ross Sea ice area flux and its dependence on cross-gate pressure gradient (from N–N/ERA-40 reanalysis) during 1992–2003. (a) Mean Mar–Nov area flux and mean winter area flux (1992–2003). Dependence of ice area flux on cross-gate pressure gradient from (b) N–N and (c) ERA-40.



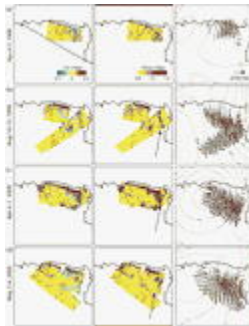
[Click on thumbnail for full-sized image.](#)

FIG. 7. Monthly anomalies in cross-gate pressure gradient and mean Ross Sea SLP between 1979 and 2002 in N-N and ERA-40 reanalyses. (a) Anomalies in monthly cross-gate pressure gradient. (b) Anomalies in mean Ross Sea SLP. (c) Maps of trends in SLP anomalies. Boxes show the domain over which the mean trends are computed. (Note different color scales in the N-N and ERA-40 trend maps).



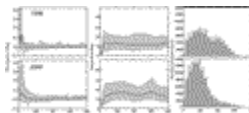
[Click on thumbnail for full-sized image.](#)

FIG. 8. Differences in the anomalies in the cross-gate SLP gradient associated with the two extreme phases of SO ($SOI > 0$ and $SOI < -1$) and SAM ($SAMI > 0.8$ and $SAMI < -0.3$) in the N-N and ERA-40 reanalyses.



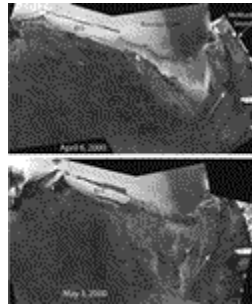
[Click on thumbnail for full-sized image.](#)

FIG. 9. Sample daily deformation (divergence and shear) and motion fields of the ice cover from RADARSAT observations sampled on 10-km grid: (a) 4 Apr 1998, (b) 14 Aug 1998, (c) 6 Apr 2000, (d) 3 May 2000. (Isobar contour intervals: 4 hPa.) Arrows point to area of convergence due to opposing easterly ice motion along the Ross Ice Shelf and westerly ice motion driven by drainage wind from the Scott Coast.



[Click on thumbnail for full-sized image.](#)

FIG. 10. Summary of all small-scale daily deformation results (divergence and motion) of the Ross Sea ice as a function of distance from coast and ice front.



[Click on thumbnail for full-sized image.](#)

FIG. 11. RADARSAT imagery of the Ross Sea polynya on 6 Apr 2000 and 3 May 2000. Iceberg B15 (area: $\sim 11 \times 10^3 \text{ km}^2$; $295 \text{ km} \times 37 \text{ km}$) during its initial stages of separation (calving) from the ice shelf. White arrows point to area of convergence due to opposing northward ice motion along the Ross Ice Shelf and eastward ice motion driven by drainage winds from the Scott Coast (RADARSAT imagery © CSA 2004).

Corresponding author address: Dr. R. Kwok, Jet Propulsion Laboratory, California Institute of Technology, 4800 Oak Grove Dr., Pasadena, CA 91109. E-mail: ron.kwok@jpl.nasa.gov